Quantum molecular dynamics simulations of methane-water mixture at extreme conditions in Uranus and Neptune

Ronghao Hu ⬤, Yifeng Li ⬤, Chuan Wang ⬤, Yang Hu ⬤, and Meng Lv[*]

College of Physics, Sichuan University, Chengdu 610064, People's Republic of China;
Key Laboratory of Radiation Physics and Technology, Ministry of Education, Chengdu 610064, People's Republic of China;
and Key Laboratory of High Energy Density Physics and Technology, Ministry of Education, Chengdu 610064, People's Republic of China

Based on first-principles molecular dynamics simulations, the equation of state and Hugoniot curve of a methane-water mixture are investigated at relevant conditions in Uranus and Neptune. Under a strong shock wave, the compression ratio of the methane-water mixture is significantly higher than that of pure methane. Calculations of the pair-correlation function show that methane molecules are dissociated by ionized water above 4000 K. Above 6000 K, the methane and water molecules are completely dissociated, and many short-lived chemical species such as H_3O and OH ions, C–O bonds, and free H atoms are formed. These results may provide a reasonable material basis for the unusual magnetic fields and the thin-shell dynamo models in Uranus and Neptune. The temperature and density ranges of our simulations are also relevant to dynamic shock experiments, and the results may provide reasonable models for future laboratory studies.

I. INTRODUCTION

Methane and water are very abundant in our universe. Most methane and water molecules are "frozen" as a fluid mixture in the "ice" layers inside the interiors of giant planets, where the pressure ranges from 20 GPa (10^9 Pa) to 600 GPa and the temperature ranges from 2000 to 8000 K [1]. Methane-water mixtures undergo progressive chemical changes as a function of the increasing density and temperature along the planetary radius [2,3], and these changes are thought to be the cause of the unusual magnetic fields in Uranus and Neptune [4,5]. The methane hydrate is also a potential clean energy source for the 21st century [6]. A better understanding of methane-water mixtures in the relevant range of pressures and temperatures is important for planetary science and material science.

To simplify planetary models, laboratory and simulation studies were previously focused on the properties of individual components. Given the large H_2O component in exoplanets, the properties of water, such as the equation of state (EOS) [7–10], Hugoniot curves [11–13], and electrical and thermal properties [14–17], have been investigated in detail at extreme conditions. These results have shown signs of a superionic phase at 3.8 g/cm^3 and 700 GPa, indicating that this water model can be used as the standard for modeling Neptune, Uranus, and "hot Neptune" exoplanets [11]. Methane is also one of the major components in "ice" layers of these planets. The properties of pure methane under extreme conditions, such as the EOS [18–22], Hugoniot curves [23–25], pair-correlation functions [18,26], and electrical conductivity and optical properties [27–31], are investigated using dynamic shock experiments and density

functional molecular dynamics (DFT-MD) simulations. These studies have found that diamondlike configurations occur at ultrahigh pressures and temperatures, proving that the dehydrogenation reactions prevent methane from changing to a superionic state [14,26,28,30–32]. However, chemical interactions caused by the pressure and temperature may change the properties of a mixture relative to its individual components and lead to sedimentation or upwelling of a major constituent in "ice" layers, which could have a large influence on the thermal evolution of the ice giants. For example, Lee *et al.* [33] studied CH_4-H_2O mixtures and demonstrated that, compared to pure substances, mixing leads to the progressive ionization of methane and that the samples become electronically conductive. Liu *et al.* [34] used spectroscopic experiments and *ab initio* simulations to demonstrate that, under mild pressure conditions of 7.4 GPa and 300 K, mixtures of water and ammonia react and produce, in part, NH_4^+ and OH^-. They explain this surprising coexistence of neutral/charged species as resulting from a topological frustration between different ions. Huang *et al.* [35] used DFT-MD simulations to characterize the behavior of H_2 and H_2O molecules in the deep interiors of Uranus and Neptune, finding the existence of H_3O at 4.3 g/cm^3. This can give rise to anomalous nondipolar and nonaxisymmetric fields consistent with the thin-shell dynamo model proposed for these planets. Bethkenhagen *et al.* [36] performed DFT-MD simulations on a ternary mixture of methane, ammonia, and water at a ratio of 2:1:4, and they developed a new adiabatic model of Uranus with an inner layer of nearly pure ices.

In this paper, we perform DFT-MD simulations of methane-water mixtures for density and temperature ranges relevant to conditions in the interiors of Uranus and Neptune. The Hugoniot curve and the EOS of a methane-water mixture are obtained. The pair-correlation function, the

[*]Corresponding author: lvmengphys@scu.edu.cn

mean-squared displacement (MSD), and the electronic band gap are analyzed to explain the obtained Hugoniot curve and the EOS. Under a strong shock wave, the compression ratio of the methane-water mixture is significantly higher than that of pure methane. Methane molecules are dissociated by ionized water above 4000 K. Above 6000 K, the methane and water molecules are completely dissociated, and many short-lived chemical species such as H_3O and OH ions, C–O bonds, and free H atoms are formed. These results may provide a reasonable material basis for the unusual magnetic fields and the thin-shell dynamo models in Uranus and Neptune. The temperature and density ranges of our simulations are also relevant to dynamic shock experiments, and the results may provide reasonable models for future laboratory studies.

II. COMPUTATIONAL METHODS

The simulations are carried out with the DFT-MD software Vienna *ab initio* simulation package (VASP) 5.4.4 [37,38]. In these simulations, the electrons receive a full quantum-mechanical treatment via solving the Kohn-Sham equations for a set of orbitals and energies within a plane-wave finite temperature density functional theory [39] formulation, where the electronic states are populated according to the Fermi-Dirac distribution at the temperature T_e. The all-electron projector augmented wave (PAW) [40] method is adopted, and the exchange-correlation energy is described employing the functional of Perdew, Burke, and Ernzerhof (PBE) of the generalized gradient approximation (GGA) [41]. The PBE functional is a commonly used approximation in MD simulations, which is computationally less expensive and can agree with the results of the functional of Heyd, Scuseria, and Ernzerhof within an acceptable error range [42–45]. Electronic excitations are accounted for using Fermi-Dirac smearing [46].

Simulations are undertaken at 56 different temperature density conditions. The densities range from 1 to 3 g/cm^3. Temperatures range from 1000 to 15 000 K. Following Ref. [33], each simulation cell consisted of 13 methane molecules and 19 water molecules in a cubic cell with temperature controlled by a Nose-Hoover thermostat. Each simulation lasted for at least 2 ps, and in some cases up to 8 ps. The supercells are constructed in the following way. We constructed a periodic single cell containing two methane molecules and three water molecules. Then, the single cell is extended to 2×2×2 supercells, and redundant molecules are eliminated to maintain a ratio of 13:19 [47].

The numerical convergence of the DFT-MD simulations is an important issue, which is verified by performing convergence tests on five parameters: the number of K-points, the ion step convergence criterion, the energy cutoff of the plane-wave basis, the number of bands, and the time step [47]. The effects of these five parameters on pressure and internal energy are tested separately by keeping other parameters fixed. According to the results of convergence tests, the ion step convergence criterion is set to 1×10^{-5} eV, the energy cutoff for the plane-wave basis is set to 900 eV, the time step is set to 0.2 fs, the number of bands is set to 192, and the density of a single K-point in K-space is high enough so that the Brillouin zone is sampled with a single Γ point

to reduce computational costs. The change in internal energy and pressure by using higher precision parameters is less than 2‰ [47].

The Hugoniot curve, which is the set of end states that can be reached from some given initial states, is calculated using the Rankine-Hugoniot relation [48]:

$$H = (e - e_0) + \tfrac{1}{2}(p + p_0)(\rho^{-1} - \rho_0^{-1}) = 0, \qquad (1)$$

where e and e_0 are the internal energies for final and initial states, p and p_0 are the pressures for final and initial states, and ρ and ρ_0 are the densities for final and initial states. The initial states are obtained with DFT-MD simulation by setting temperature $T_0 = 1000$ K and $\rho_0 = 1$ g/cm^3, and $e_0 = -4.538$ eV/atom and $p_0 = 6.27$ GPa are then calculated. The Hugoniot points are determined in the following way [18]. For a given temperature, DFT-MD simulations are performed at different densities. Then, the internal energies e, the pressure p, and the Hugoniot function H are calculated and fitted to cubic functions of temperature T. The zero point of function H is found numerically, and the corresponding final states (ρ, T, e, p) that satisfy Eq. (1) are then obtained.

III. RESULTS

A. Hugoniot curve and EOS

DFT-MD simulations are performed at various density and temperature conditions, which are marked in Fig. 1(a). The Hugoniot curve in the density-temperature space is also shown in Fig. 1(a), which connects all possible final thermodynamic states generated by a planar shock wave to the initial thermodynamic state. For pure methane, the slope of Hugoniot curve $\partial T / \partial \rho$ first decreases and then increases as temperature increases [26]. For the mixture, the slope of the Hugoniot curve increases monotonically as temperature increases. Under 3000 K, methane molecules remain relatively stable while small amounts of unstable H_3O^+ and OH^- are generated. Around 3000–4000 K, the slope of the Hugoniot curve increases markedly and the ionization phase transition occurs in the mixture. A large amount of molecular species, especially methane species, starts dissociating, forming parts of C–C and C–O bonds and transient H_2 molecules, indicating that the mixture further transforms to the fluid phase. Above 5000 K, the molecules are completely dissociated, and many ion species exist for short periods of time. The hydrogen atoms become highly diffusive, leading to a band-gap closure, which will be discussed in Secs. III B and III C. This indicates that the metallization phase transition of methane-water occurs and that the system changes into a plasma state. A preliminary analysis of the Hugoniot curve indicates that the fluid and plasma phases of this mixture in ice giant planets can only exist at temperatures above 4000 K [14]. The calculated Hugoniot curve in density-pressure space is shown in Fig. 1(b). The pressure increases almost exponentially with the density. At low compression ratio ρ/ρ_0, the Hugoniot curve of the mixture is closer to that of the pure methane [26]. At a high compression ratio, the Hugoniot curve is closer to that of the pure water [11,49]. For strong shock waves, the fluid methane-water mixture shows strong dissociation, as in the case of water molecules. We noted that chemical interactions between water and methane molecules
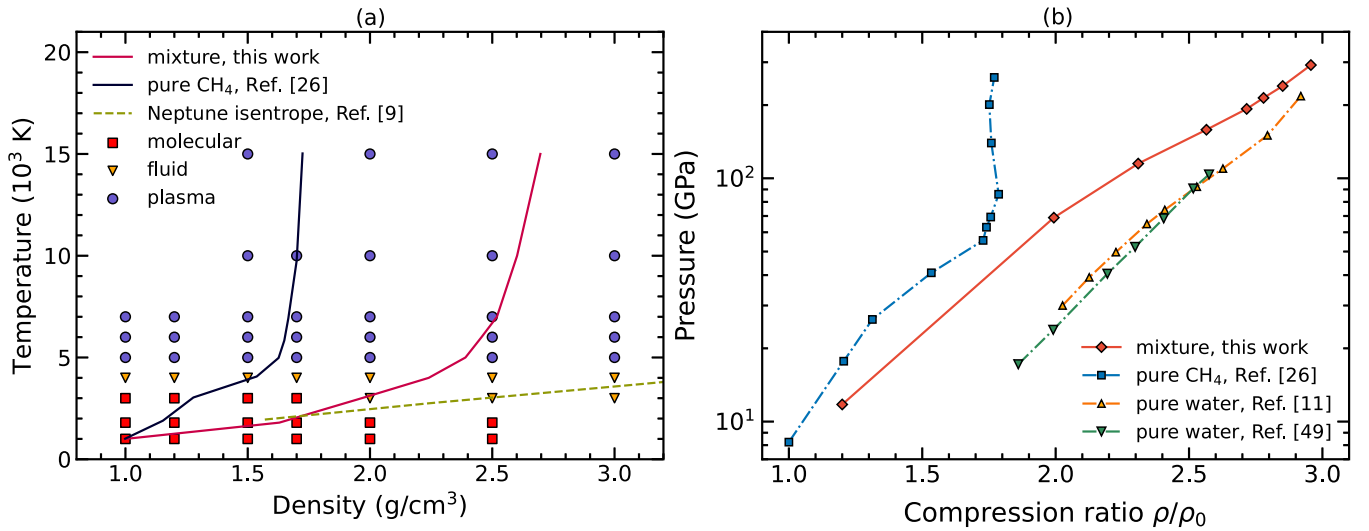
FIG. 1. (a) Principal Hugoniot curves in density-temperature space based on the DFT-MD simulations. The symbols show the density and temperature conditions for our simulations, and they mark the molecular, fluid, or plasma state. The Hugoniot curve for methane from Ref. [26] and the Neptune isentrope from Ref. [9] are also shown in the figure. (b) Pressure as a function of the compression ratio ρ/ρ_0, along the shock Hugoniot curves. The results of previous simulations for methane (from Ref. [26]) and water (from Refs. [11] and [49]) are also shown for comparison.

occur after mixing, which changes their properties under high-temperature and high-pressure conditions.

The EOS data of the methane-water mixture are shown in Fig. 2(a) and tabulated in the Supplemental Material [47]. The phase transitions of the mixture are also indicated by the EOS data. In Fig. 2(a), $\partial p/\partial T$ decreases at a temperature of 4000 K and densities of 1.5 and 2.0 g/cm³, but it is still positive. The methane starts dissociating under the catalysis of water. When the temperature rises to 6000 K, $\partial p/\partial T$ rises again, and this identifies an insulator-to-metal transition. Compared to Ref. [33], the dissociation temperature and pressure region are similar to those of pure methane, with the energy primarily

depending on the bonding number of the light and heavy nuclei [36]. We did not observe a region with $\partial p/\partial T < 0$ at densities of 1.0–3.0 g/cm³, which indicates that the composition of the mixture has a significant influence on its thermodynamic properties and that the mixture could not form a stable polymer, such as pure methane, after dissociation.

In addition, the phase diagram of the methane-water mixture can help us understand the thermal evolution of Uranus and Neptune. It is generally believed that giant planets are made up of several different layers of matter. Material deep in the planetary "ice layers" appears to be fluid, and such layers are usually convective, often as a result of a hotter internal
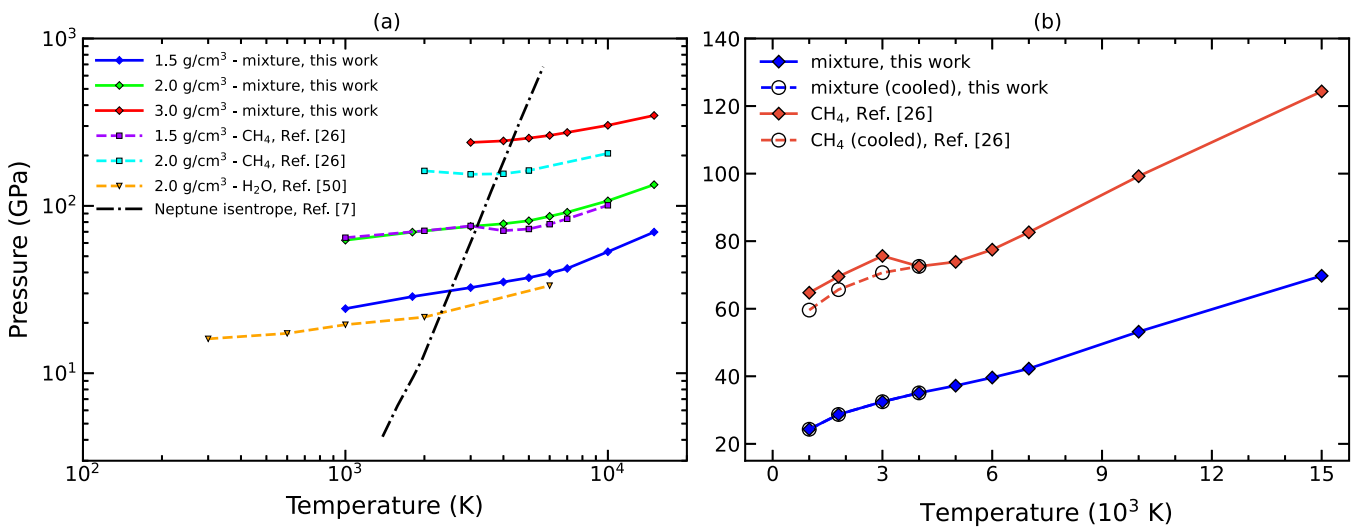

FIG. 2. (a) EOS for the methane-water mixture as relevant for the interiors of Uranus and Neptune. For comparison, the present DFT-MD simulation results are provided together with previous simulations of methane (from Ref. [26]), water (from Ref. [50]), and the isentrope of Neptune (from Ref. [7]). (b) Pressure-temperature relations of the methane-water mixtures that have been heated and cooled from 4000 K. The red lines indicate methane simulations [26], and the blue lines indicate methane-water mixture simulations. The solid lines indicate the heating process, and the dashed lines indicate the cooling process. The densities of the methane-water mixtures and pure methane are 1.5 g/cm³.
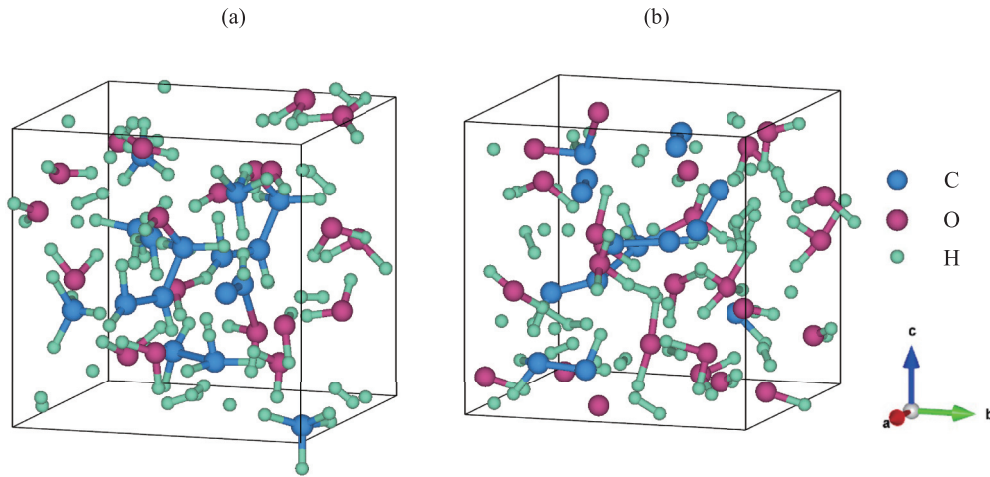
FIG. 3. (a) Snapshot from the MD simulation at 1.5 g/cm^3 and 4000 K. C atoms are depicted in blue, O atoms are depicted in wine, and H atoms are depicted in green. The borders of the simulation cell are depicted by solid lines. The initial configurations of the CH$_4$ molecules collapse, and some C–C and C–O bonds are formed. (b) Snapshot from MD simulations at 1.5 g/cm^3 and 7000 K. The initial configurations of all molecules collapse, part of H$_3$O-OH ion pairs, and free hydrogen atoms are formed.

to surface heat flow. Our EOS curves cross the isentropic line of Neptune, which indicates that the mixing entropy increases with increasing temperature at the same density. The molecules of the mixture tend to evolve into multiple unstable chemical species. The phase-transition temperature of the methane-water mixture is lower than that of the Uranus-Neptune ice rock thermodynamic boundary, which leads to the dissolution of rock layer material into "ice" layers being favorable under these thermodynamic conditions [15]. The phase transition behavior of the fluid mixture also helps to prove the rationality of the complex planetary models of Uranus and Neptune. For example, the thin-shell generator model proposed by metallization can be used to explain the complex magnetic-field structure [35,51]. The phase transition of fluid mixture can shorten the planet's cooling behavior, which is useful to explain the thermal evolution in an "ice" planet [52]. The EOS data can also be used to estimate the size, age, and cooling rate of some water-rich exoplanets, such as Kepler-68b [53].

Previous simulations of pure methane show that a polymeric state is formed around 4000 K and leads to a region with $\partial p/\partial T < 0$ in the p-T relation curve [26]. After cooling from 4000 K, the polymeric state remains and exhibits lower pressures than the molecular state of methane [26]. We simulated the heating and cooling of the methane-water mixture at a density of 1.5 g/cm^3. The cooling simulations are carried out as follows: we first run the simulations at 4000 K for 8 ps, then rescale the particle velocities to a certain temperature, and continue the simulation for 1.5 ps. As shown in Fig. 2(b), the heating and cooling curves for the mixture are identical. No polymeric state is formed, and the molecular dissociation process is reversible. After cooling, the unstable C–C and C–O bonds in the mixture are found to be reduced to stable H$_2$O and CH$_4$ molecules. The activation barrier of the reduction to stable molecules is small. Conversely, the activation barrier of stable molecules to the ionic phase is larger, therefore it is necessary to break the binding of the activation energy via heating [33].

B. Ionic structure and pair-correlation function

To interpret the EOS data, we extracted simulation snapshots after 3 ps at a density of 1.5 g/cm^3 and temperatures of 4000 and 7000 K, and we examined the behavior of the mixture in the ionic and plasma phases, respectively. In Fig. 3(a), it is observed that at 4000 K, water molecules exhibit high reactivity as a chemical solvent, leading to the dissolution and dissociation of methane molecules into CH$_3^+$, with the formation of C–C and C–O bonds catalyzed by ionic water. This results in the formation of a small transient complex consisting of two to four carbon atoms. In addition, the original C–H and O–H bonds in the methane-water mixture are broken, H is highly diffusible, and a small amount of transient H$_2$ molecule formation can be observed. At the same temperature, the diffusion of H can also be observed in the simulation of pure water, which is considered by Schwegler [54] as a sign of the formation of the fluid phase. Different from the findings of [26], no carbon chain saturated hydrocarbons are found in the mixture, indicating that the presence of water inhibited the polymerization of methane.

As shown in Fig. 3(b), at 7000 K, we can see that the water molecules are nearly completely dissociated, and some water molecules form short-lived H$_3$O$^+$ and OH$^-$ ions. Because of the higher simulated temperature, the degree of dissociation in the mixture is more severe than that in pure water [55]. C–C bonds form and break in a dynamic manner, leading to transient carbon complexes with carbon atoms in different coordinations [33]. The number of free H and transient H$_2$ molecules increased significantly compared to the situation at 4000 K, and the dissociation of the two molecules is complete. All of the ionic species formed at this temperature are transient and unstable.

It is apparent that the chemical reactions of water and methane in the plasma and fluid phases have a significant influence on the physical and chemical properties of the mixture. Unlike the case of pure methane, most of the chemical bonds cannot be stable. Therefore, we need to modify ice giant planet models based on the behavior of pure
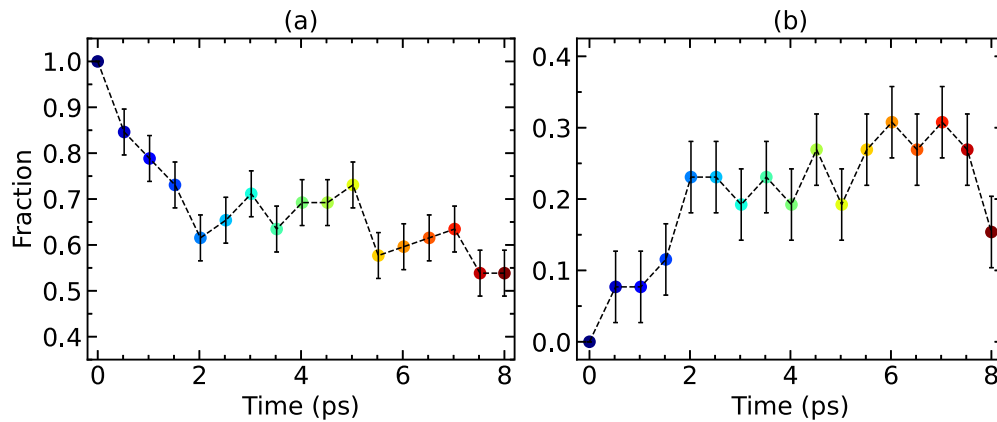
FIG. 4. Evolution of the fraction of (a) C–H and (b) C–C bonds during the MD simulation at 4000 K and 1.5 g/cm^3. The decrease of C–H bonds and the increase of C–C bonds measure how many molecules collapse into ionic species, which is illustrated in Figs. 3(a) and 3(b).

hydrocarbons and the implied diamond formation. We also suggest that combustible ice and other "ices" be used as samples in laser-heated diamond anvil cell experiments and in dynamic shock experiments [30,56].

We now study the clusters in the fluid mixture to extract more details concerning the dissociation process of methane in the ionic phase. Different polymerization reactions can be detected by analyzing the changes in the proportions of several chemical bonds. In Fig. 4, we set the bonding distance of the C–C bond to 1.8 Å, that of the C–H bond to 1.4 Å, and that of the C–O bond to 1.7 Å to analyze the transition process of the methane-water mixture. The ratio of the C–H bond number decreased to 1/2 of the ratio at the beginning of the simulation at 7 ps, which indicated that the CH$_4$ molecules are continuously decomposed and that the proportion of unstable C–C and C–O clusters formed after decomposition is increasing. When the simulation reached 8 ps, the fluid mixture was formed.

To explain the structural changes in the mixture in the fluid and plasma phases, we calculated the pair-correlation functions for each pair of atom type, which quantify the probability of finding an atom of a given type at a given distance from a reference atom. All pair-correlation functions are computed at a density of 1.5 g/cm^3. In Figs. 5(a) and 5(b), at 1000 K, there are peaks in $g_{CH}(r)$ and $g_{OH}(r)$ at 1.1 and 1 Å, respectively, representing the equilibrium nuclear distances between the C–H bonds of methane and the O–H bonds of the methane and water molecules. However, increasing the temperature leads to a gradual decrease in the peak value, indicating that a large amount of methane and water molecules are dissociated. The $g(r)$ peak value of C–H at 4000 K is only 1/3 of that at 1000 K, which means that the dissociation of methane is nearly complete. This finding is consistent with the snapshot in Fig. 3(a).

In Figs. 5(c) and 5(d), we find that, when the temperature reaches 4000 K, the original peaks in $g_{CO}(r)$ and $g_{CC}(r)$ diminish gradually near 1.3 Å, while new peaks appear near 3 Å, which corresponds to the length of the C–C and C–O bonds in the fluid mixture. Finally, at 15 000 K, when the mixture transforms to the plasma phase, no new peaks can be observed. However, the broadening of $g_{CO}(r)$ and $g_{CC}(r)$

illustrates that most of the chemical bonds at this temperature are unstable, and that breaking and reformation of the chemical bonds occurs very frequently.

Compared to Ref. [26], as shown in Figs. 5(e) and 5(f), the peak $g_{CH}(r)$ value of the mixture of 1.1 Å at 2.0 g/cm^3 is approximately twice that of pure methane. Therefore, the presence of water inhibits the fracture of the C–H bonds and prevents the formation of complex carbon species at 4000 K, which confirms the results in the visualization in Fig. 3(a). Compared to pure methane, a new peak value of $g_{HH}(r)$ forms near 0.8 Å, implying that the liquid mixture can decompose into more hydrogen molecules than pure methane at 4000 K. In conclusion, the formation of diamond after the phase transformation of pure methane is not incompatible with the current results but is challenged by microscopic evidence [33] because important differences in the molecular behaviors of the two compositions can be clearly seen by combining the snapshot analysis results and the correlation functions. Therefore, we describe the behavior of the fluid mixture in the range of 4000–5000 K as an ionic phase rather than a polymer phase in Refs. [18] and [26].

C. Mean-squared displacement and electrical properties

The formation of a large number of unstable molecular groups in the snapshot of the fluid mixture can also be understood via the MSD of the atoms in Fig. 6. For example, at 1000 K, the MSDs of the three types of atoms tend to gradually become stable after the initial ballistic region within 1 ps, indicating that the molecules of the mixture are stable at 1000 K and that all atoms are near their equilibrium positions. At 4000 K, in the 8-ps simulation, the MSD of the H atoms is still increasing, while those of the C and O atoms are near 10 Å^2, which provides a numerical explanation for the existence of free H in the fluid phase and the formation of transient H$_2$ molecules. In a simulation of pure water [50], H atoms start diffusing at temperatures above 1400 K, while O atoms oscillate around the bcc lattice sites, and the system behaves like a superionic solid. This means that the sharp increase in the melting curve slope is caused by the dissociation of water molecules and the diffusion of hydrogen atoms. At higher
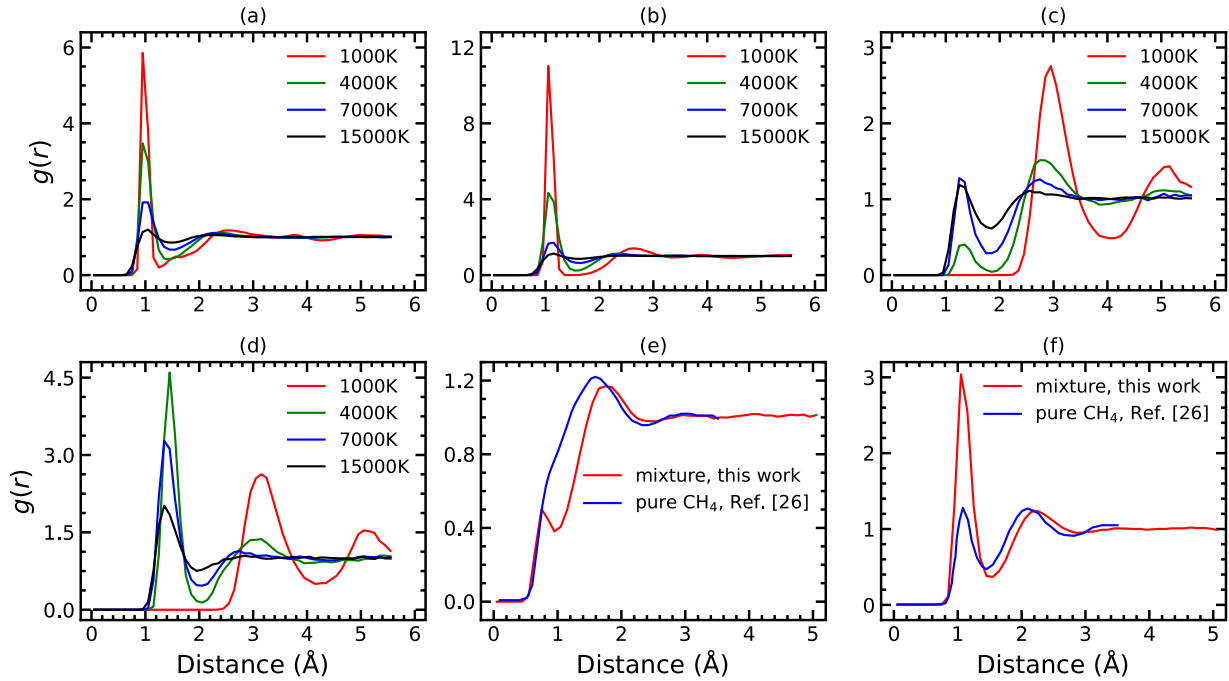
FIG. 5. Pair-correlation functions, $g(r)$, as a function of the distance between the atom pairs at different temperature conditions. (a) C–H, (b) O–H, (c) C–O, and (d) C–C pair-correlation functions at 1.5 g/cm^3. While the temperature increases, the intensities of the C–C and C–O peaks at 1.3 Å increase markedly at 4000 K and decrease again at 10 000 K. (e) H–H and (f) C–H pair-correlation functions at 4000 K and 2.0 g/cm^3. The pair-correlation function for methane [26] is also provided for comparison in panels (e) and (f).

temperatures (7000 K), the free H atoms are already in the superionic state, and the MSDs of the C and O atoms increase continuously within 8 ps, which implies that large-scale diffusion has also taken place. Therefore, the dissociation of the water and methane molecules is complete.

Finally, we calculated the electron band gap averaged over the trajectory of the fluid mixture after MD simulations to analyze the conductivity. As shown in Fig. 7, when the temperature is below 3000 K, the system remains in the insulating state and the band gap is 3 eV or more. Compared to Ref. [26], at 3000 K, the band gap is lower than 3 eV, which implies that, compared to pure methane, the mixture will transform into a semiconductor at a lower temperature. We observed a

snapshot after simulating for 3 ps at this temperature, and we found that a small amount of methane molecules are dissociated into CH$_3$ groups and free H atoms. When the temperature is above 4000 K, the band gap decreases further and the system evolves into a conductor.

The above findings provide some understanding of the possible physical origin of the dynamo model and the unusual magnetic fields of the ice giant planets. The phase transitions of multicomponent systems in the "ice layers" change greatly under extreme conditions. Accordingly, the combination of dynamic compression techniques and theoretical calculations can lead to an improved understanding of the detailed structures of these unusual magnetic fields in terms of
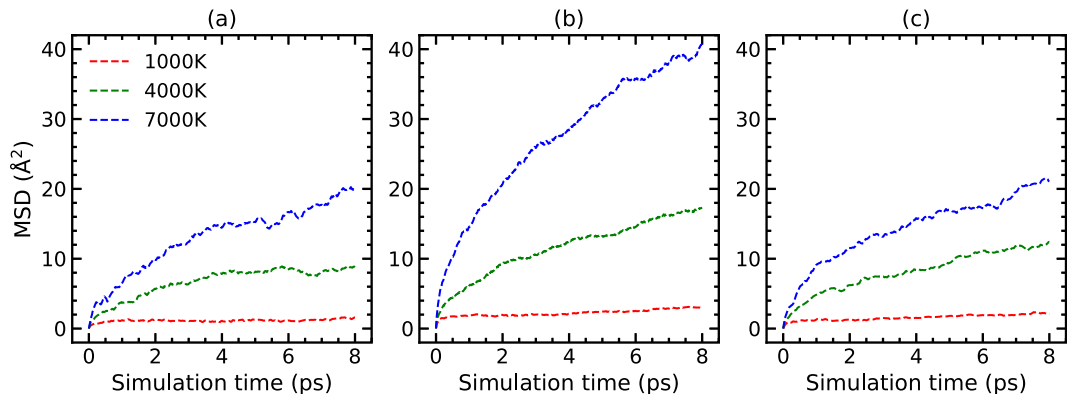

FIG. 6. MSD as a function of simulation time at 1.5 g/cm^3. The three temperatures represent the molecule, fluid, and plasma states for (a) C, (b) H, and (c) O atoms. When the temperature increases, the MSD increases rapidly.
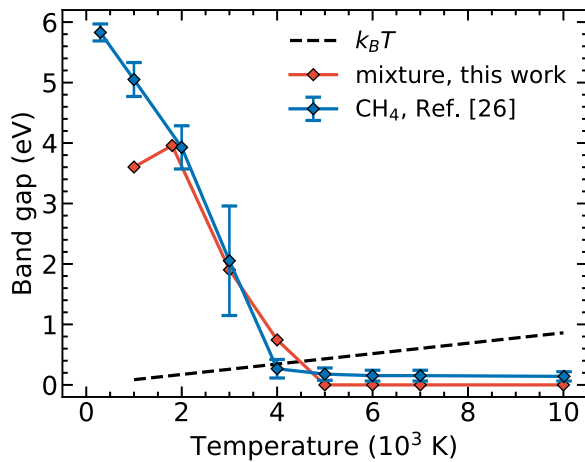
FIG. 7. Electron average band gap of the fluid mixture during the simulations at 1.5 g/cm^3. The band gap of methane [26] is also provided. When $T > 4000$ K, the electron band gap is less than the temperature, which implies that the samples are transformed into the metallic state.

the component materials. The highly mobile H atoms and the ionic conductivity should significantly influence the chemical, electronic, and transport properties of "ice" planets such as Uranus and Neptune.

IV. CONCLUSIONS

Based on DFT-MD simulations, we characterized and analyzed the molecular, fluid, and plasma states in a temperature-density range of 1000–15 000 K and 1–3 g/cm^3 for a methane-water mixture. The compression ratio of the mixture is much higher than that of pure methane under a strong shock wave, which indicates that such mixtures are dissociated under extreme conditions. Such dissociation leads to an instability of the chemical bonds in the fluid and plasma states, which can allow a better understanding of interior models of exoplanets.

When the methane-water mixture is in the fluid or plasma phase, the molecules dissociate into many H_3O^+ and OH^- ions, C–O bonds, and free H atoms. This transformation is accompanied by an increase in the ionic conductivity. These results may provide a reasonable material basis for the unusual magnetic fields and the thin-shell dynamo models in Uranus and Neptune. The P-T ranges of our simulations are also relevant to conditions in dynamic shock experiments, and the results may provide reasonable models for future laboratory studies.

[1] W. B. Hubbard and J. J. Macfarlane, J. Geophys. Res. **85**, 225 (1980).

[2] W. B. Hubbard, Science **214**, 145 (1981).

[3] H. B. Radousky, A. C. Mitchell, and W. J. Nellis, J. Chem. Phys. **93**, 8235 (1990).

[4] R. Holme and J. Bloxham, J. Geophys. Res. **101**, 2177 (1996).

[5] N. F. Ness, M. H. Acuña, K. W. Behannon, L. F. Burlaga, J. E. P. Connerney, R. P. Lepping, and F. M. Neubauer, Science **233**, 85 (1986).

[6] Z. Tan, P. Ge, and L. Pingkuo, Sustainability **8**, 520 (2016).

[7] R. Redmer, T. R. Mattsson, N. Nettelmann, and M. French, Icarus **211**, 798 (2011).

[8] K. K. M. Lee, L. R. Benedetti, R. Jeanloz, P. M. Celliers, J. H. Eggert, D. G. Hicks, S. J. Moon, A. Mackinnon, L. B. Da Silva, D. K. Bradley, W. Unites, G. W. Collins, E. Henry, M. Koenig, A. Benuzzi-Mounaix, J. Pasley, and D. Neely, J. Chem. Phys. **125**, 014701 (2006).

[9] M. French, T. R. Mattsson, N. Nettelmann, and R. Redmer, Phys. Rev. B **79**, 054107 (2009).

[10] M. Millot, S. Hamel, J. Rygg, P. Celliers, G. Collins, F. Coppari, D. Fratanduono, R. Jeanloz, D. Swift, and J. Eggert, Nat. Phys. **14**, 297 (2018).

[11] M. D. Knudson, M. P. Desjarlais, R. W. Lemke, T. R. Mattsson, M. French, N. Nettelmann, and R. Redmer, Phys. Rev. Lett. **108**, 091102 (2012).

[12] T. R. Mattsson and M. P. Desjarlais, Phys. Rev. Lett. **97**, 017801 (2006).

[13] N. Giovambattista, H. Eugene Stanley, and F. Sciortino, Phys. Rev. E **72**, 031510 (2005).

[14] M. French, T. R. Mattsson, and R. Redmer, Phys. Rev. B **82**, 174108 (2010).

[15] H. F. Wilson and B. Militzer, Astrophys. J. **745**, 54 (2012).

[16] F. Grasselli, L. Stixrude, and S. Baroni, Nat. Commun. **11**, 3605 (2020).

[17] J. W. Biddle, V. Holten, J. V. Sengers, and M. A. Anisimov, Phys. Rev. E **87**, 042302 (2013).

[18] D. Li, P. Zhang, and J. Yan, Phys. Rev. B **84**, 184204 (2011).

[19] M. Veit, S. K. Jain, S. Bonakala, I. Rudra, D. Hohl, and G. Csányi, J. Chem. Theor. Comput. **15**, 2574 (2019).

[20] R. B. Jadrich, C. Ticknor, and J. A. Leiding, J. Chem. Phys. **154**, 244307 (2021).

[21] S. Jiang, T. Guo, Y.-X. Yu, and J. Hu, Int. J. Thermophys. **43**, 22 (2022).

[22] A. E. Gleason, D. R. Rittman, C. A. Bolme, E. Galtier, H. J. Lee, E. Granados, S. Ali, A. Lazicki, D. Swift, P. Celliers, B. Militzer, S. Stanley, and W. L. Mao, Sci. Rep. **12**, 715 (2022).

[23] T. Qi and E. J. Reed, J. Phys. Chem. A **116**, 10451 (2012).

[24] W. J. Nellis, F. H. Ree, M. van Thiel, and A. C. Mitchell, J. Chem. Phys. **75**, 3055 (1981).

[25] A. V. Kudinov, S. A. Gubin, and Y. A. Bogdanova, J. Phys.: Conf. Ser. **1686**, 012081 (2020).

[26] B. L. Sherman, H. F. Wilson, D. Weeraratne, and B. Militzer, Phys. Rev. B **86**, 224113 (2012).

[27] W. J. Nellis, D. C. Hamilton, and A. C. Mitchell, J. Chem. Phys. **115**, 1015 (2001).

[28] H. Hirai, K. Konagai, T. Kawamura, Y. Yamamoto, and T. Yagi, Phys. Earth Planet. Inter. **174**, 242 (2009).

[29] L. Spanu, D. Donadio, D. Hohl, E. Schwegler, and G. Galli, Proc. Natl. Acad. Sci. USA **108**, 6843 (2011).

[30] D. Kraus, J. Vorberger, A. Pak, and N. J. Hartley, Nat. Astron. **1**, 606 (2017).

[31] N. J. Hartley, S. Brown, T. E. Cowan, E. Cunningham, T. Döppner, R. W. Falcone, L. B. Fletcher, S. Frydrych, E. Galtier, E. J. Gamboa, A. Laso Garcia, D. O. Gericke, S. H. Glenzer, E. Granados, P. A. Heimann, H. J. Lee, M. J. MacDonald, A. J. MacKinnon, E. E. McBride, I. Nam *et al.*, Sci. Rep. **9**, 4196 (2019).

[32] H. F. Wilson, M. L. Wong, and B. Militzer, Phys. Rev. Lett. **110**, 151102 (2013).

[33] M. S. Lee and S. Scandolo, Nat. Commun. **2**, 185 (2011).

[34] C. Liu, A. Mafety, J. A. Queyroux, C. W. Wilson, H. Zhang, K. Béneut, G. Le Marchand, B. Baptiste, P. Dumas, and G. A. Garbarino, Nat. Commun. **8**, 1065 (2017).

[35] P. Huang, H. Liu, J. Lv, Q. Li, C. Long, Y. Wang, C. Chen, R. J. Hemley, and Y. Ma, Proc. Natl. Acad. Sci. USA **117**, 5638 (2020).

[36] M. Bethkenhagen, E. R. Meyer, S. Hamel, N. Nettelmann, M. French, L. Scheibe, C. Ticknor, L. A. Collins, J. D. Kress, and J. J. a. Fortney, Astrophys. J. **848**, 67 (2017).

[37] G. Kresse and J. Furthmüller, Phys. Rev. B **54**, 11169 (1996).

[38] G. Kresse and J. Hafner, Phys. Rev. B **47**, 558 (1993).

[39] S. Mazevet, P. Blottiau, J. D. Kress, and L. A. Collins, Phys. Rev. B **69**, 224207 (2004).

[40] G. Kresse and D. Joubert, Phys. Rev. B **59**, 1758 (1999).

[41] J. P. Perdew, K. Burke, and M. Ernzerhof, Phys. Rev. Lett. **77**, 3865 (1996).

[42] J. Heyd, G. E. Scuseria, and M. Ernzerhof, J. Chem. Phys. **118**, 8207 (2003).

[43] J. Heyd, G. E. Scuseria, and M. Ernzerhof, J. Chem. Phys. **124**, 219906 (2006).

[44] M. French and R. Redmer, Phys. Plasmas **18**, 043301 (2011).

[45] N. Nettelmann, B. Holst, A. Kietzmann, M. French, R. Redmer, and D. Blaschke, Astrophys. J. **683**, 1217 (2008).

[46] N. D. Mermin, Phys. Rev. **137**, A1441 (1965).

[47] See Supplemental Material at http://link.aps.org/supplemental/10.1103/PhysRevB.107.174108 for the constructed supercell, results of numerical convergence tests, and calculated EOS data.

[48] Y. Zeldovich and Y. Raizer, *Physics of Shock Waves and High-Temperature Hydrodynamic Phenomena* (Academic, New York, 1966).

[49] A. Mitchell and W. Nellis, J. Chem. Phys. **76**, 6273 (1982).

[50] E. Schwegler, M. Sharma, F. Gygi, and G. Galli, Proc. Natl. Acad. Sci. USA **105**, 14779 (2008).

[51] N. F. Ness, M. H. Acuña, L. F. Burlaga, J. E. P. Connerney, R. P. Lepping, and F. M. Neubauer, Science **246**, 1473 (1989).

[52] N. Nettelmann, K. Wang, J. Fortney, S. Hamel, S. Yellamilli, M. Bethkenhagen, and R. Redmer, Icarus **275**, 107 (2016).

[53] L. Zeng and D. Sasselov, Astrophys. J. **784**, 96 (2014).

[54] E. Schwegler, G. Galli, F. Gygi, and R. Q. Hood, Phys. Rev. Lett. **87**, 265501 (2001).

[55] A. F. Goncharov, N. Goldman, L. E. Fried, J. C. Crowhurst, I.-F. W. Kuo, C. J. Mundy, and J. M. Zaug, Phys. Rev. Lett. **94**, 125508 (2005).

[56] L. R. Benedetti, J. H. Nguyen, W. A. Caldwell, H. Liu, M. Kruger, and R. Jeanloz, Science **286**, 100 (1999).